A microporous surface containing Si₃N₄/Ta microparticles of PEKK exhibits both antibacterial and osteogenic activity for inducing cellular response and improving osseointegration

Xinglong Hu [a], Shiqi Mei [a], Fan Wang [a], Songchao Tang [a], Dong Xie [b], Chao Ding [a], Wenli Du [a], Jun Zhao [c, ***], Lili Yang [b, **], Zhaoying Wu [d], Jie Wei [a, *]

[a] *Key Laboratory for Ultrafine Materials of Ministry of Education, East China University of Science and Technology, Shanghai, 200237, China*
[b] *Spine Center, Department of Orthopaedics, Shanghai Changzheng Hospital, Second Military Medical University, Shanghai, 200003, China*
[c] *Shanghai Key Laboratory of Stomatology, Shanghai Research Institute of Stomatology, Department of Orthodontics, Ninth People's Hospital Affiliated to Shanghai Jiao Tong University, School of Medicine, Shanghai, 200011, China*
[d] *School of Biomedical Engineering, Sun Yat-sen University, Guangzhou, Guangdong, 510006, China*

ARTICLE INFO

ABSTRACT

As an implantable biomaterial, polyetherketoneketone (PEKK) exhibits good mechanical strength but it is biologically inert while tantalum (Ta) possesses outstanding osteogenic bioactivity but has a high density and elastic modulus. Also, silicon nitride (SN) has osteogenic and antibacterial activity. In this study, a microporous surface containing both SN and Ta microparticles on PEKK (STP) exhibiting excellent osteogenic and antibacterial activity was created by sulfonation. Compared with sulfonated PEKK (SPK) without microparticles, the surface properties (roughness, surface energy, hydrophilicity and protein adsorption) of STP significantly increased due to the SN and Ta particles presence on the microporous surface. In addition, STP also exhibited outstanding antibacterial activity, which inhibited bacterial growth *in vitro* and prevented bacterial infection *in vivo* because of the presence of SN particles. Moreover, the microporous surface of STP containing both SN and Ta particles remarkably induced response (e.g., proliferation and differentiation) of rat bone mesenchymal stem (rBMS) cells *in vitro*. Furthermore, STP significantly improved new bone regeneration and osseointegration *in vivo*. Regarding the induction of cellular response *in vitro* and improvement of osseointegration *in vivo*, the microporous surface containing Ta was better than the surface with SN particles. In conclusion, STP with optimized surface properties activated cellular responses *in vitro*, enhanced osseointegration and prevented infection *in vivo*. Therefore, STP possessed the dual biofunctions of excellent osteogenic and antibacterial activity, showing great potential as a bone substitute.

1. Introduction

As a type of high-property polymeric biomaterial, poly-aryletherketone (PAEK) is gradually becoming a leading biomaterial in orthopedic application due to its high mechanical strength, good biocompatibility and biostability as well as elastic modulus similarity to human bone, which can avoid stress shielding that often occurs in the use of metal implants leading to implantation failure [1]. Poly-etherketoneketone (PEKK) and polyetheretherketone (PEEK) are two representative types of PAEK family [1,2]. PEEK exhibits great potential for bone repair owing to its superior mechanical properties, and has been extensively used in spinal fusion, trauma, dental and joint replacement, and cranio-maxillofacial repair [3]. Recently, PEKK, as another representative PAEK family material, is being increasingly researched and developed as a potential implantable material for orthopedic application because it shows better potential for orthopedic and spinal as well as dental application than PEEK [4]. In comparison with PEEK, PEKK possesses two ketone bonds leading to versatile

chemistry, and structural variation between the amorphous phase and semi-crystalline, thereby exhibiting certain advantages (e.g., favorable mechanical properties and thermal stability) [5]. In addition, PEKK has received a permit from the Food and Drug Administration of the United States, and thereby acceptance by the biomedical manufacturers for making implants [6]. Unfortunately, as a biologically inert material, PAEK displays poor osteogenic bioactivity and cannot integrate with the host bone, but causes the development of fibrous tissue layer around PAEK implants [7]. The formation of fibrous tissue encapsulation between PAEK and the host bone tissue lacks long-term stability, which finally leads to loosening, and even failure of implants [7].

For permanent orthopedic devices, favorable integration with host bone (known as osseointegration) is necessary for the primary fixation and long-term stability of implants. Therefore, osseointegration of PAEK is considered as the gold standard for successful implantation *in vivo* [8]. Several strategies (e.g., surface modification with physical, chemical and biological ways) have been applied to increase the surface bioactivity of PAEK (e.g., PEEK) to facilitate new bone regeneration and osteointegration, such as plasma treatment, NaOH-etched/boron-doped nanohydroxyapatite coating or a bone morphogenetic protein-2 immobilized collagen coating on PEEK [9–11]. However, these surface modification strategies may not be sufficient to produce biomedical implants with excellent osteogenic bioactivity and stability for clinical applications [12,13]. Furthermore, peri-implantitis caused by pathogenic bacteria invasion is the most common complication leading to implantation failure [14]. The attachment of pathogenic bacteria on the implant surface can easily cause bacterial colonization, and further induce a sequence of inflammatory reactions (bacterial infection) that eventually result in the failure of implants [15]. Thus, it is beneficial for the implant surface possessing osteogenic bioactivity for promoting bone regeneration and antibacterial activity for preventing infection.

Recently garnering much attention, Tantalum (Ta) has excellent osteogenic bioactivity and is generally applied as bone implants, artificial joints, dental implants and cranioplasty plates [16]. Historically, Ta has been considered as biologically inert implant that was highly biocompatible and unreactive in the human body [17]. However, recent reports indicated that Ta could stimulate osteoblast response (e.g., proliferation, differentiation and mineralization) because of its high friction factor, high surface energy and hydrophilicity, and micron/nano roughness [18]. Furthermore, Ta significantly promoted osteoblast proliferation and mineralization in comparison with other metallic biomaterials, such as titanium (Ti) and alloys, and cobalt-based alloys [19]. Moreover, porous Ta allowed bone tissue in-growth to achieve favorable osseointegration, thereby improving the initial fixation and long-term stability of implants [20]. However, Ta is not as popular as other metallic biomaterials (e.g., Ti and alloys) for fabricating orthopedic implants probably because of its significantly higher density and elastic modulus than those of human bone [21]. Moreover, the difficulty of processing and high cost limits the wide application of bulk Ta implants [21].

As a type of non-oxide ceramic, silicon nitride (Si_3N_4, SN) has been investigated and developed as biomedical implants for orthopedic application since the 1990s, due to its exceptional osteoconductivity, biocompatibility and biostability as well as antibacterial activity [22–26]. As an implantable biomaterial with osteogenic bioactivity, SN has been developed for orthopedic devices, such as cages for spinal fusion, component of artificial joints. Previous studies demonstrated that the surface chemistry of SN could change from a silica-rich to a principally silicon-amine composition that might influence the responses of both bacteria and cells/tissues [25]. It was reported that the SN surface possessed inherently resistant to bacteria that could inhibit biofilm formation, indicating excellent antibacterial activity [22,27,28]. The antibacterial mechanism of the SN surface is due to the presence of $-NH_2$ group and the formation of a weak alkaline microenvironment caused by dissolution of SN in the physiological environment [23,25, 28].

This investigation aimed to design a PEKK-based implantable material with dual biofunctions of antibacterial and osteogenic activity that could prevent infection and activate cellular response/bone regeneration for orthopedic implant application. A microporous surface containing SN/Ta microparticles on PEKK (STP) was fabricated by sulfonation reaction. Consequently, the surface features (e.g., composition, micro-morphology, hydrophilicity, roughness) of STP were comprehensively characterized. In addition, the *in vitro* antibacterial activity against *Staphylococcus aureus (S. aureus) and Escherichia coli (E. coli)* and *in vivo* anti-infective property of STP was evaluated. Moreover, the cellular response (such as adhesion, proliferation, differentiation and osteogenesis related gene expressions) of rat bone mesenchymal stem (rBMS) cells to STP were evaluated *in vitro*. New bone regeneration and osseointegration of STP were also investigated *in vivo*.

2. Materials and methods

2.1. Preparation of specimens

Ta particles, purchased from Grandview Materials Inc., USA, and SN particles (β phase), purchased from Adamas, China, were used as the powder samples. The concentrated sulfuric acid suspension with SN/Ta particles was obtained by putting SN and Ta microparticles into sulfuric acid (Aldrich Co., USA) with concentration of 95%–98% at room temperature. The sulfuric acid suspension with SN/Ta particles was magnetically stirred for 3 h and ultrasonically stirred for 3 h to disperse the particles. By the same method, the concentrated sulfuric acid suspensions with either SN or Ta particles were made as controls. Polyetherketoneketone (PEKK) powders, purchased from Arylmax K7500, Polymics Co., USA, were washed with ethanol and deionized (DI) water for 1 h. The PEKK powders were then dried in an oven at 50 °C for 12 h. Dense PEKK samples were fabricated by cold pressing-sintering methods. Specifically, PEKK powders were placed in stainless steel molds (Φ12 × 2 mm, Φ4 × 6 mm and Φ1 × 12 mm) and then pressed by tablet machine (YP-40T, Tianjin Nuoleixinda Technology, China) with a pressure of 5 MPa. The specimens from tablet pressing were sintered in the muffle furnace (at 355 °C for 6 h). Afterwards, the specimens were ground with 2000 mesh abrasive paper; then the ground PEKK was soaked into sulfuric acid without particles (SPK, control), with 20 wt% SN particles (SNP, control), with 20 wt% Ta particles (TAP, control), and with 20 wt% SN/Ta particles (STP, the mass ratio of SN and Ta = 1:1) for 15 min at room temperature, respectively. Subsequently, the samples were immersed in DI water at 100 °C for 24 h to remove residual sulfuric acid. Finally, the modified samples (labeled as SPK, SNP, TAP and STP) were ultrasonically cleaned by ethanol and DI water for three repetitions and then dried (at 60 °C) for 12 h to obtain the specimens.

2.2. Characterization of specimens

The morphology and particle size of both SN and Ta were characterized by transmission electron microscope (TEM, JEM-2100F, JEOL Co., Japan). The chemical groups and phase composition of SPK, SNP, TAP and STP were detected using Fourier transform infrared spectrophotometry (FTIR, Nicolet 6700, Thermo Co., USA) and X-ray diffraction (XRD, XRD-6100, Shimadzu Co., Japan). The surface morphology and roughness of the specimens were characterized by field-emission scanning electron microscopy (FESEM, S4800, Hitachi Co., Japan) and three-dimensional (3D) laser scanning confocal microscope (VK-X200, Keyence, Japan). The elemental composition and distribution of the specimens were investigated by energy-dispersive X-ray spectrometry (EDS, SDD550, IXRF Co., USA). The hydrophilicity of the specimens was evaluated by measuring the water contact angles. The surface energy of specimens was calculated using water and diiodomethane contact angles according to the Owens two-liquid method [29]. The contact angles of water and diiodomethane for the samples were determined utilizing a contact angle measurement (XG-CAMC3, Shanghai Xuanyichuangxi

Table 1
Primers applied for RT-PCR.

Gene	Forward primer sequence (5′–3′)	Reverse primer sequence (5′–3′)
ALP	GGATCAAAGCAGCATCTTACCAG	GCTTTCCCATCTTCCGACACT
OPN	GTCCCTTGCCCTGACTACTCT	GACATCTTTTGCAAACCGTGT
OCN	CAGACAAGTCCCACACAGCA	CCAGCAGAGTGAGCAGAGAG
Runx2	ATCCAGCCACCTTCACTTACACC	GGGACCATTGGGAACTGATAGG
GAPDH	CCTGCACCACCAACTGCTTA	GGCCATCCACAGTCTTCTGAG

Industial Equipment Co., China). Briefly, 2 μL of DI water was dropped onto the samples surface at room temperature, and the images were captured using camera when the droplet stabilized. SPK, SNP, TAP and STP were immersed in simulated body fluid (SBF) and kept in a constant temperature oscillator (HZQ-F160A, Shanghai Yiheng Scientiifc Instruments Co., China) at 37 °C. The pH values of the solution were measured with a pH meter (FE20, Mettler Toledo, Switzerland) after the samples were soaked in SBF for 0.5, 1, 3, 7, 10, and 14 d.

2.3. Proteins adsorption on specimens

Proteins adsorption on the specimen surface was investigated using Micro Bicinchoninic Acid (μBCA) assay reagent kit following the manufacturer's instructions. In brief, the specimens (SPK, SNP, TAP and STP) were placed into a 24-well plate, then 1 mL of bovine serum albumin (BSA, 5 mg/mL) or fibronectin (Fn, 30 μg/mL) was introduced on the specimen surface and incubated for 6 h at 37 °C. After that, the specimens were rinsed carefully with phosphate buffered saline (PBS) to remove the unadsorbed proteins. Afterwards, the adsorbed proteins were eluted with 2% sodium dodecyl sulfate (SDS) under shaking (at 37 °C) for 6 h. The solution was collected, and the protein mass in SDS solutions was obtained using a μBCA assay kit by measuring the absorbance at 562 nm, and the adsorbed protein density (D_a) was acquired using equation (1) as follows:

$$D_a = \frac{M_a}{S} \tag{1}$$

where M_a represented the mass of proteins adsorption (μg) on each group (SPK, SNP, TAP and STP), and S represented the surface area (cm^2) of each group.

2.4. Antibacterial activity of specimens in vitro

The bacteria counting assay was performed to investigate the antibacterial activity of the samples. Before the experiments, the specimens were sterilized in 75 vt% ethanol aqueous solution for 24 h and dried on a super clean bench. Afterwards, 0.2 mL of *Staphylococcus aureus* (*S. aureus,* gram-positive bacterium, ATCC 25923) or *Escherichia coli* (*E. coli*, gram-negative bacterium, ATCC 25922) suspension with a density of 1×10^7 colony forming units (CFU mL^{-1}) were inoculated on each specimen and incubated at 37 °C for 24 h. Subsequently, the specimens were transferred into sterilized centrifugal tubes containing 4 mL PBS. After that, the tubes were agitated intensely using a vortex mixer (HMS-350, HengAo Technology Co., China) to detach the bacteria from the specimens. Afterwards, 60 μL of the diluted suspension of dissociated bacteria was inoculated onto nutrient agar, and a sterilized scraper was utilized to spread the suspension on the plates uniformly. After incubation for 24 h (at 37 °C), the colonies were counted (the National Standard of China GB/T 4789.2–2010 protocol), and PEKK without surface modification was set as a control. The antibacterial percentage (R_b) was acquired according to the following equation:

$$R_b = \frac{N_0 - N_1}{N_0} \times 100\% \tag{2}$$

where N_0 was the average number of the bacteria colonies on the control group (PEKK) and N_1 was the average number of the bacteria colonies on SPK, SNP, TAP and STP.
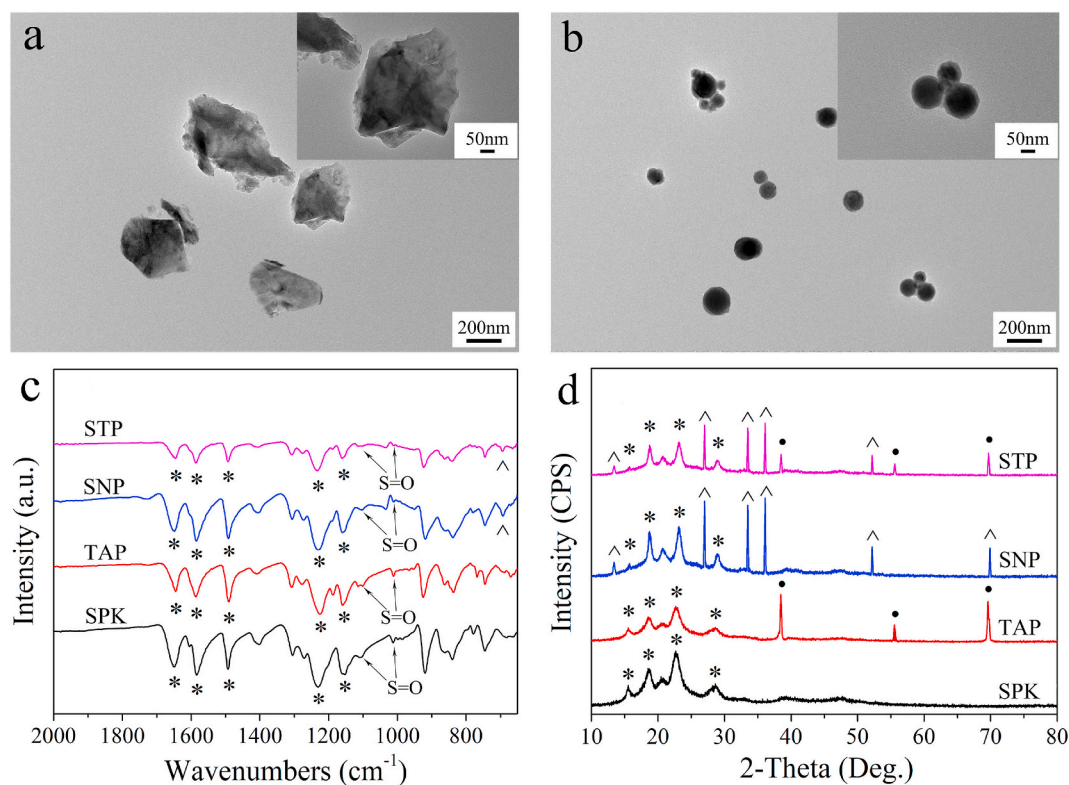

Fig. 1. TEM image of SN (a) and Ta (b) particles, and FTIR spectra (c) and XRD spectra (d) of SPK, SNP, TAP and STP; * represents PEKK characteristic peaks, ^ represents SN characteristic peaks, and ●represents Ta characteristic peaks.
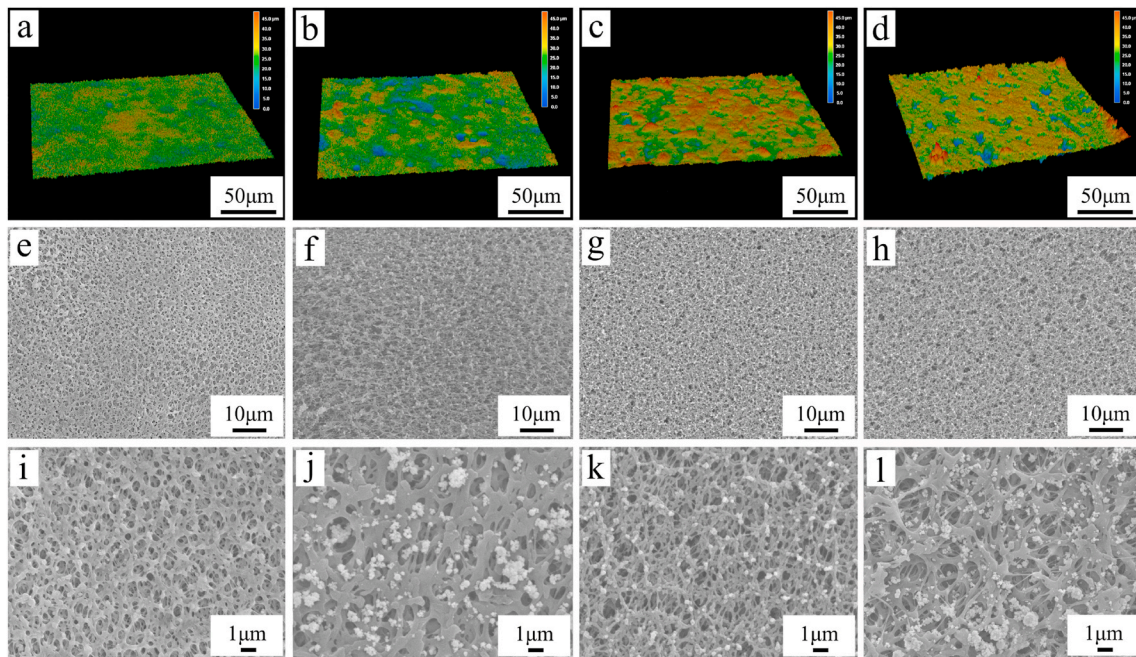
Fig. 2. Three-dimensional images of laser microscope of surface morphology of SPK (a), SNP (b), TAP (c) and STP (d) and SEM images of SPK (e, i), SNP (f, j), TAP (g, k) and STP (h, l) under different magnification.
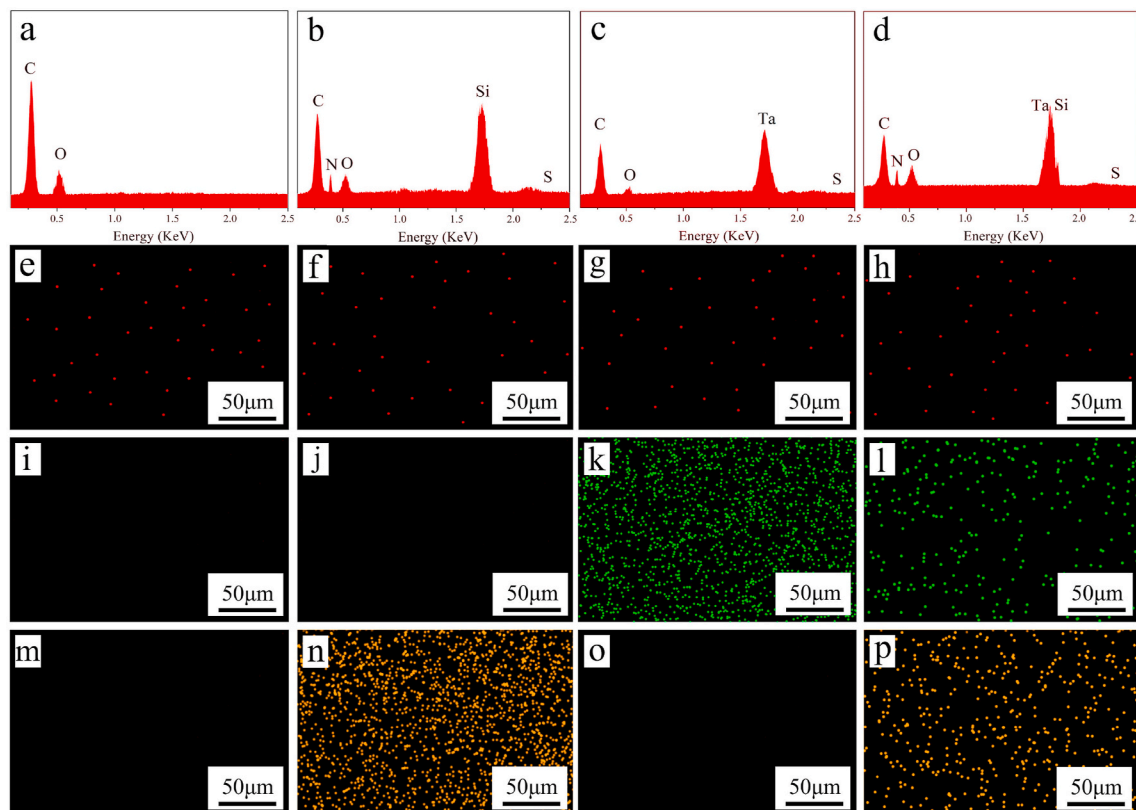

Fig. 3. EDS elemental spectra of SPK (a), SNP (b), TAP (c) and STP (d), and EDS elemental mapping of SPK (e, i, m), SNP (f, j, n), TAP (g, k, o) and STP (h, l, p), and the element distribution of sulfur in red (e, f, g, h), Ta in green (i, j, k, l) and silicon in yellow (m, n, o, p). (For interpretation of the references to colour in this figure legend, the reader is referred to the Web version of this article.)

2.5. Cell responses to specimens in vitro

Rat bone mesenchymal stem cells (rBMS cells, from Stem Cell Bank, Chinese Academy of Science) were cultured with α-Minimum Essential Medium (α-MEM, Gibco, USA) containing 10% heat-inactivated fetal bovine serum (FBS, Gibco, USA), 1% antimicrobial of penicillin/streptomycin (HyClone, USA) at 37 °C in a 5% CO_2 incubator. Before culturing, the samples were sterilized using ethylene oxide, and then
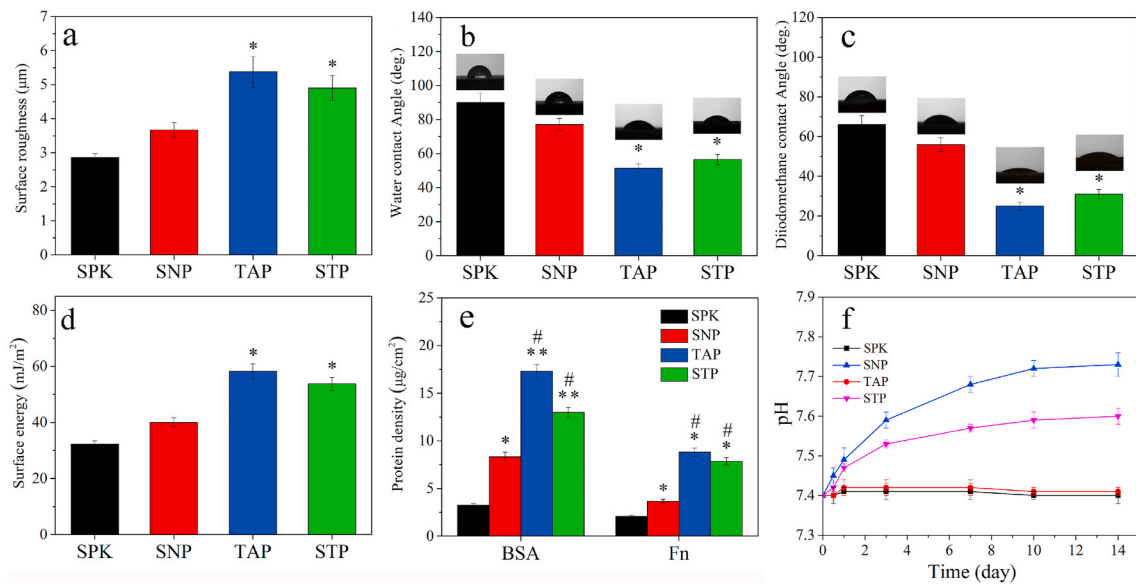
Fig. 4. Surface roughness (a), water contact angle (b), diiodomethane contact angle (c), and surface energy (d) of the specimens (SPK, SNP, TAP, and STP), and adsorption (e) of BSA and Fn on the specimens, and change of pH value (f) in solution after the specimens' immersion in SBF for different time (n = 3, * was $p < 0.05$, ** was $p < 0.01$, in comparison with SPK; # was $p < 0.05$, in comparison with SNP).
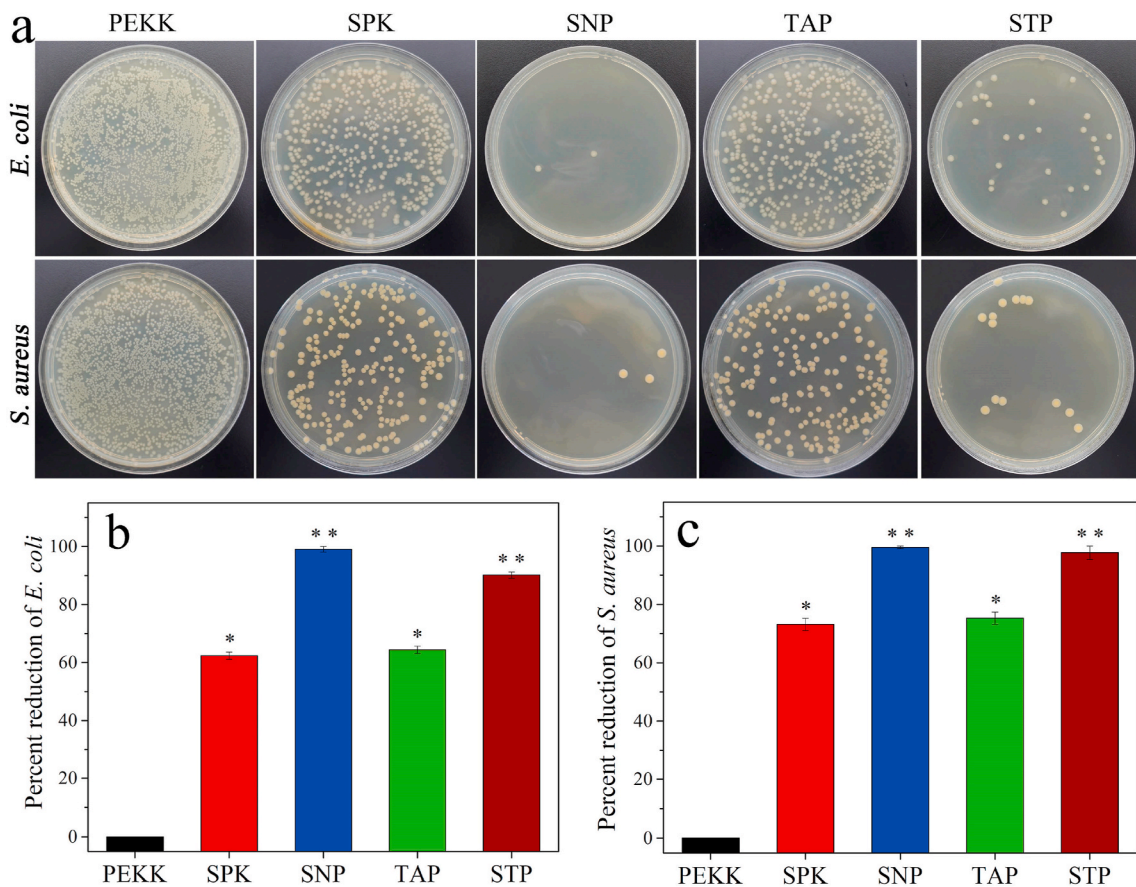

Fig. 5. Photos (a) of *S. aureus* and *E. coli* colonies cultured on different samples, and percent reduction of *S. aureus* (c) and *E. coli* (b) (n = 3, * was $p < 0.05$, in comparison with PEKK; ** was $p < 0.01$, in comparison with PEKK).

placed in a 24-well plate. The rBMS cells (5 × 10^4 cells/well) were seeded onto the specimens to evaluate the adhesion and proliferation as well as osteogenic differentiation of rBMS cells. The culture medium was refreshed every two days.

2.5.1. Cell adhesion and morphology

For cell adhesion, the rBMS cells were cultured on the sample surface for 1 day and 3 days. At the end of each time point, the culture medium was removed, and the samples were rinsed thrice with PBS and then
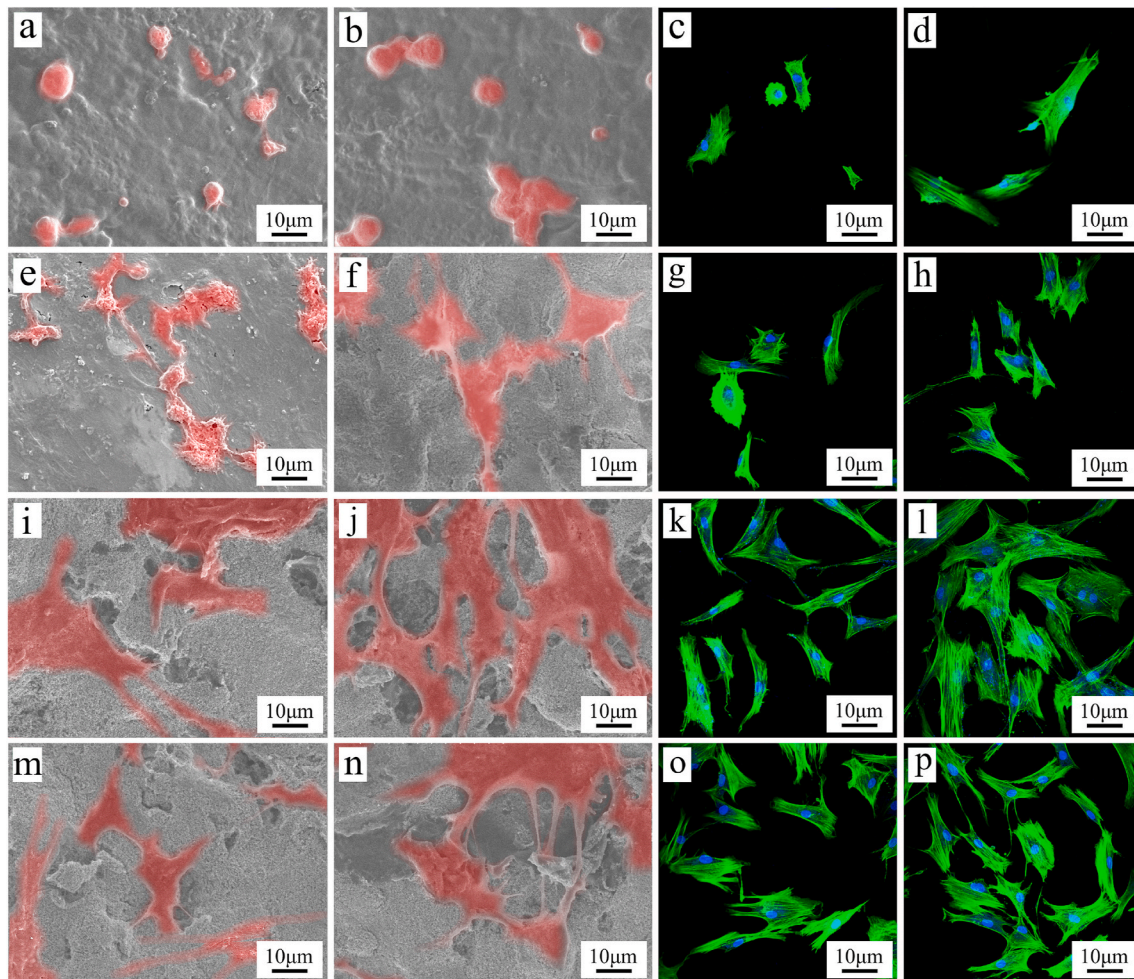
Fig. 6. SEM images of rBMS cells on SPK (a, b), SNP (e, f), TAP (i, j), and STP (m, n), and CLSM photographs of the cells on SPK (c, d), SNP (g, h), TAP (k, l), and STP (o, p) at day 1 (a, c, e, g, i, k, m, o) and 3 (b, d, f, h, j, l, n, p) after culturing.

immobilized with 4% paraformaldehyde solution overnight. Subsequently, the fixed cells were incubated using fluorescein isothiocyanate-Phalloidin (FITC-Phalloidin, Yeasen Biotech, China) for 1 h and 2-(4-Amidinophenyl)-6-indolecarbamidine dihydrochloride (DAPI, Sigma, USA) for 10 min in darkness. Cell morphology was visualized using confocal laser-scanning microscopy (CLSM, from Nikon A1R, Japan). The cell morphology of rBMS cells on SPK, SNP, TAP and STP was observed using SEM after dehydrated in ascending concentrations of ethanol solutions (30%, 50%, 75%, 90%, 95% and 100%, v/v) for 10 min and drying at 25 °C.

2.5.2. Cell proliferation and osteogenic differentiation

After incubation for 1, 3 and 7 days, cell proliferation was evaluated using Cell Counting Kit-8 assay (CCK-8, Dojindo Co., Japan). Specifically, at the end of each time point, the culture medium was removed, and the samples were gently rinsed thrice with 1 mL of PBS and moved to new 24-well plates, and then incubated for 5 h after being supplemented with α-MEM containing CCK-8 at a ratio of 10:1 (v/v). Afterwards, the supernatant (100 μL/well) was transferred into 96-well plates, and optical density (OD) values were determined by a microplate reader (from Cytation 5, BioTek, USA) at a wavelength of 450 nm with 620 nm as the reference.

After incubation of rBMS cells on the specimens for 7, 10 and 14 days, the culture medium was removed, and the cells were rinsed thrice by 1 mL of PBS, then lysed with 1% Triton X-100, and the lysate of rBMS cells was obtained, followed by centrifugation at 12000 rpm for 5 min. The supernatant was incubated utilizing *p*-nitrophenyl-phosphate

(pNPP, 2 mg/mL, Sigma, USA) for 30 min (at 37 °C). After that, the reaction was terminated by NaOH solution (0.1 mol/L). The absorbance of Alkaline phosphatase (ALP) was determined with a Microplate Reader (SPECTR Amax 384, from Molecular Devices, USA) at 405 nm wavelength. The ALP activity was presented as absorbance at 405 nm divided by the total protein quantity, which was assessed by μBCA assay kit and a series of BSA standards.

ALP staining was performed using a BCIP/NBT ALP kit (Beyotime, China). Briefly, the rBMS cells were plated in 24-well plates and cultured for 14 days with different samples. After fixation with 4% paraformaldehyde solution for 30 min, the cells were incubated in a mixture of nitro-blue tetrazolium and 5-bromo-4-chloro-3-indolylphosphate. Extracellular matrix (ECM) mineralization of rBMS cells was analyzed on day 21 using Alizarin-Red staining. At the end of the incubation time, cells were fixed with 4% paraformaldehyde solution for 30 min. The fixed cells were rinsed three times with PBS and stained with 1% Alizarin Red (Solarbio, China) for 30 min. The unbound dyes were removed by thorough washing with distilled water before the images were taken by optical microscopy.

2.5.3. Osteogenesis gene expression

The expression of osteogenic gene was evaluated by Real-time quantitative reserve transcription-polymerase chain reaction (Real-time PCR). Briefly, after 3, 7 and 14 days of culture on samples (10^5 cells/well), the total RNA was extracted from rBMS cells with Rneasy mini kit (Qiagen Co., Germany). After that, RNA (1 μg) was transcribed into complementary DNA (cDNA) using iScript cDNA Synthesis Kit (Bio-
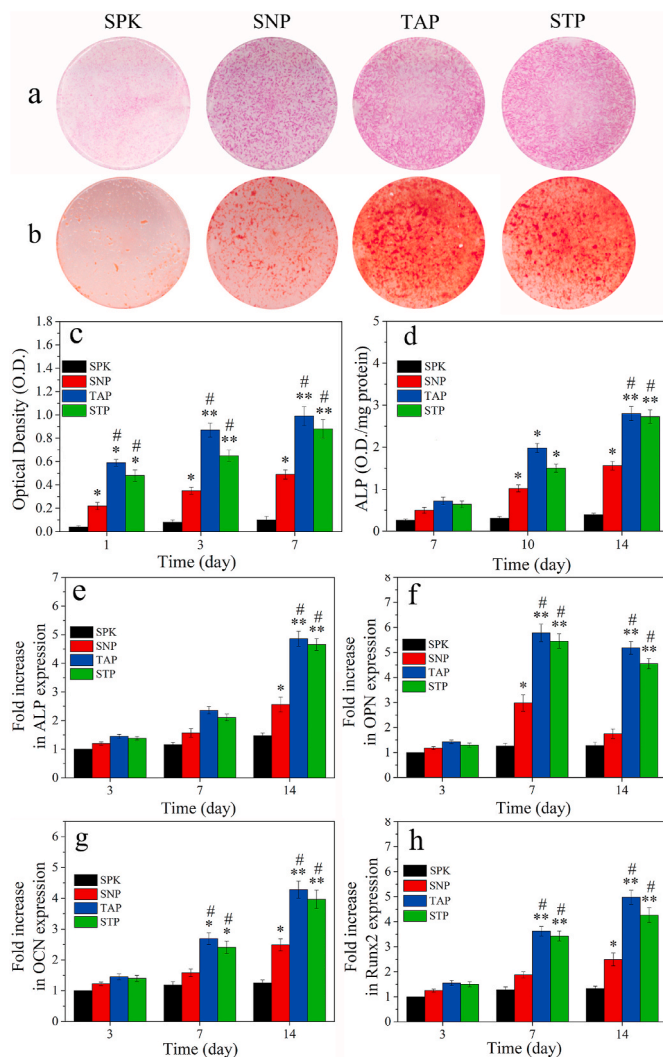
Fig. 7. ALP staining (a) of the rBMS cells with samples at day 14 after culturing; Alizarin-Red staining (b) of calcium nodules of the cells with samples at day 21 after culturing; OD value (c) and ALP activity (d) of the cells on the samples after culturing for different time; Osteogenic gene expression of ALP (e), OPN (f), OCN (g) and Runx2 (h) of rBMS cells on the samples after culturing for different time (n = 3, * was $p < 0.05$, ** was $p < 0.01$, in comparison with SPK; # was $p < 0.05$, in comparison with SNP). (For interpretation of the references to colour in this figure legend, the reader is referred to the Web version of this article.)

RAD Co., USA). Real-time PCR was carried out by Bio-Rad real-time PCR system (Bio-RAD Co., Hercules, USA). Expressions of osteogenesis gene including ALP, osteopontin (OPN), osteocalcin (OCN) and runt-related transcription factor 2 (Runx2), were normalized to that of glyceraldehyde-3-phosphate dehydrogenase (GAPDH, house-keeping gene). The primer sequences for Real-time PCR were listed in Table 1.

2.6. Animal experiments

All animal experiments were approved by Animal Research Committee of the Ninth People's Hospital affiliated to the Shanghai Jiao Tong University. Thirty male Sprague Dawley rats were used to establish the rat femur intramedullary nail infection prevention model, and surgery was performed under aseptic conditions. In addition, twenty-four beagle dogs (male) with the weight of 9–15 kg and age of 20 months were utilized to carry out the femur implantations.

2.6.1. In vivo anti-infective property

The Sprague Dawley rats were anesthetized by intraperitoneal ketamine injection (10 mg/kg, Shanghai Ziyuan Pharmaceutical Co. Ltd, China) and 2% xylazine (5 mg/kg, Bayer AG, Germany). The rat's right hind limb was shaved, and the knee joint was fixed at the maximum flexion position. After palpating the patella, a 12-mm longitudinal incision was made along the lateral side of the patella, and the layers of tissues were separated individually. The knee joint was dislocated, and the femoral condyle was fully exposed. An electric drill was used to drill along the direction of the medullary cavity at the center of the femoral condyle. After rinsing the bones with normal saline to remove debris, sterile forceps were used to implant a small cylindrical material ($\Phi 1 \times 12$ mm) immersed in S. aureus bacteria suspension at a concentration of 1×10^7 cfu/mL for 10 min, into the bone canal. Finally, bone wax was used to seal the bone, and the wound was sutured. The rats were euthanized at 14 days after surgery.

Rat femurs were imaged under operating conditions using X-ray machines (52 kV and 3.2 mAs, Digital Diagnost, Philips, Netherlands) at 14 days after surgery. For the spread plate analysis, the bone tissues of the femurs were crushed with rongeurs, and the retrieved samples from the rat femur were placed in sterilized centrifugal tubes containing 4 mL PBS. After that, the tubes were agitated intensely via a vortex mixer to detach the bacteria from samples. Afterwards, 60 μL of the diluted suspension of dissociated bacteria was inoculated onto nutrient agar, and a sterilized scraper was utilized to make the suspension evenly spread on the plates. After incubation for 24 h (at 37 °C), the colonies were counted (the National Standard of China GB/T 4789.2–2010 protocol), and PEKK without surface modification was set as a control.

2.6.2. Determination of osteogenesis and osseointegration in vivo

The aforementioned dogs were divided into four groups corresponding to SPK, SNP, TAP and STP. All surgical procedures were performed under sterile conditions, and all sample implants were sterilized by gamma radiation (15 kGv) before the surgery. After anesthetizing with an intravenous injection of 1% pentobarbital (80 mg/kg, Aldrich Co., USA), the surgical area was disinfected with iodine. Subsequently, two critical-sized defects on the bilateral epicondyle of femurs were made using a 4.0 mm diameter trephine bur, followed by insertion of the implants (4.0 mm in diameter; 6.0 mm in depth). After implantation for 4 and 12 weeks, these dogs were euthanized using overdosed pentobarbital sodium through intravenous injection. The femurs containing implants were immobilized in 4% phosphate-buffered formalin solution.

2.6.3. SRμCT and Micro-CT evaluation

The repair of bone defects was assessed by Synchrotron Radiation Micro-CT (SRμCT) at week 4 and 12 after the implantation. The SRμCT measurement was performed on the harvested femurs at beamline BL13W1 of the Shanghai Synchrotron Radiation Facility (Shanghai Synchrotron Radiation Facility, China) utilizing a monochromatic beam with an energy of 40 keV as well as an implant-to-detector distance of 0.8 m. The VG Studio software (from Volume Graphics Co., Germany) was utilized to construct 2D images from 8-bit images.

The newly formed bone tissues around the implants were determined by Micro computed tomography (Micro-CT, SkyScan 1276, Bruker, USA). The parameters of Micro-CT were set at 80 kV with a resolution of 15 μm. The 3D images were reconstructed and generated by NRecon (Skyscan Co., USA) and CTvol program (Skyscan Co., USA). The trabecular thickness (TbTh), trabecular number (TbN), bone volume/total volume (BV/TV) and bone mineral density (BMD) were determined utilizing CTAn program (Skyscan, USA).

2.6.4. Histological and bone-implant contact evaluation

The femurs were dehydrated in a series of ethanol solutions with different concentrations (70%, 80%, 85%, 90%, 95% and 100%, v/v), which were embedded in polymethyl methacrylate (PMMA). The specimens were subsequently cut into sections with a thickness of 150 μm
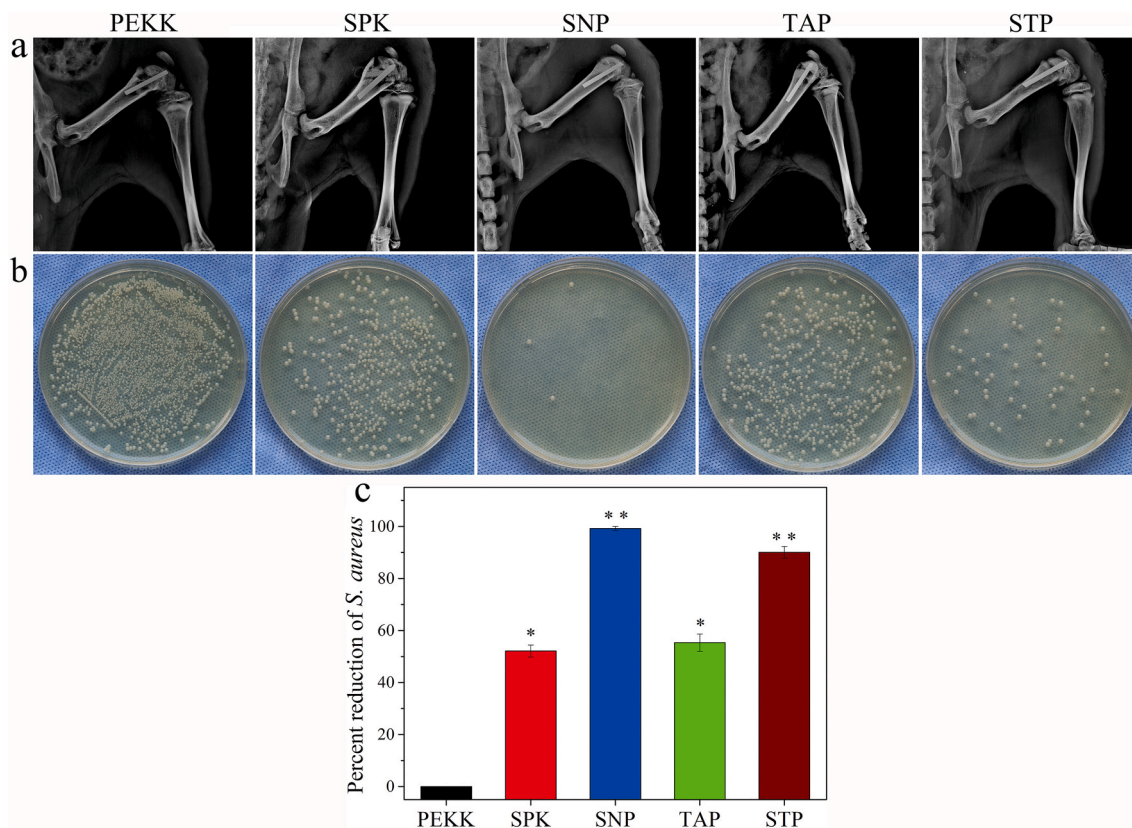
Fig. 8. X-ray images (a) of rat femurs containing implants (PEKK, SPK, SNP, TAP, STP) taken at day 14 after implantation; representative images (b) of bacterial culture detached from samples at day 14, and percent reduction of *S. aureus* (d) (n = 3, * was $p < 0.05$, in comparison with PEKK; ** was $p < 0.01$, in comparison with PEKK).

perpendicular to the long axis of the implants with a Leica SP1600 saw microtome (from Leica, Germany), and subsequently polished (thickness: 50 μm). These sections were then stained with Van Gieson's picrofuchsin staining (VG) to visualize the mineralized bone tissues (red). Simultaneously, the images were captured with an optical microscope (Olympus, WILD MP5, Japan) for histological analysis, and the index of Implant-Bone Contact (IBC) was determined using histometric analysis (GSA Image Analyser, Germany).

2.6.5. Push-out test

The bonding strength of the implant–to-bone interface was determined using a push-out test with universal testing systems (Instron 5969, USA). A bone sample with a size of approximately $\Phi 20 \times 6$ mm containing an implant ($\Phi 4 \times 6$ mm) was trimmed from the epicondyle of the femur and treated with a window operation. A special custom-designed push-rod (diameter: 2 mm) was used to fix the tested samples (SPK, SNP, TAP and STP) to ensure the test load consistent with the long axis of implants. The push-out test was implemented with the applied load ranging from 0 N to 600 N (the compression speed set as 5 mm/min). Three samples in each group were measured under the same condition. The load-displacement curve was recorded simultaneously during the pushing period, and the push-out load was defined as the maximum force value of the load-displacement curve.

2.7. Statistical analysis

Statistical analysis was performed by one-way analysis of variance. All quantitative data were expressed with the mean $\pm$ standard deviation of the results of at least three independent experiments, and p-values less than 0.05 were considered statistically significant.

3. Results

3.1. TEM, FTIR, XRD and SEM analysis

Fig. 1a showed the TEM image of SN while Fig. 1b revealed the TEM image of the Ta particles. The morphology of SN was irregular particles while Ta was spherical particles. The particle size of SN was approximately 0.5 μm while Ta was approximately 0.1 μm. Fig. 1c was the FTIR spectra of SPK, SNP, TAP and STP. The PEKK characteristic peaks could be seen in SPK, SNP, TAP and STP. In the diaryl groups, both 1232 and 1154 cm^{-1} peaks were attributed to the dissymmetric stretching vibration of C–O–C bond. The bands at 1650 and 1490 cm^{-1} were assigned to the group of diphenyl ketone. In the benzene ring, the 1586 cm^{-1} peak was related to C=C stretching vibrations. The characteristic stretching vibration bands of SN were observed at 689 cm^{-1} (Si–N–Si) in SNP and STP. In addition, the 1015 cm^{-1} peak was the symmetric stretching vibration of S=O, and the 1105 cm^{-1} peak was assigned to the dissymmetric stretching vibration of S=O. Results revealed that the sulfonic acid groups (-SO$_3$H) were introduced onto the PEKK surface after the sulfonation.

Fig. 1d reveals the XRD patterns of SPK, SNP, TAP and STP. The peaks at $2\theta = 15.4°$, $18.6°$, $22.5°$, and $28.6°$ in SPK, SNP, TAP and STP were related to the PEKK characteristic peaks. The peaks at $2\theta = 38.6°$, $55.5°$ and $69.8°$ were assigned to the characteristic peaks of Ta, which could be observed in TAP and STP. In addition, the narrow peaks at $13.4°$, $27.0°$, $33.5°$, $36.1°$, $52.2°$, and $70.0°$ were the characteristic peaks of β-phase SN, which could be observed in SNP and STP.

3.2. Surface morphology and elemental composition

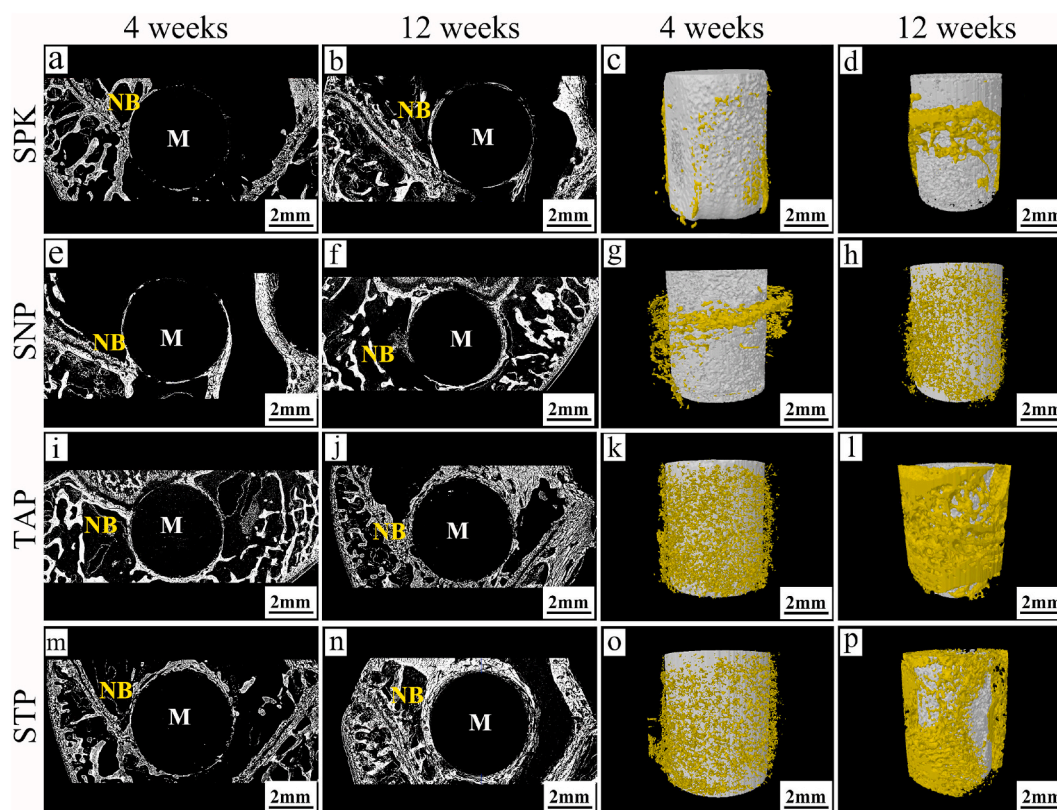Fig. 2(a–d) showed the three-dimensional (3D) images of the laser

Fig. 9. Two-dimensional (2D) reconstructed images (a, b, e, f, i, j, m, n) from SRmCT and 3D reconstructed images (c, d, g, h, k, l, o, p) from Micro-CT of the samples (SPK, SNP, TAP and STP) with new bone tissues (in yellow) at week 4 (a, c, e, g, i, k, m, o) and 12 (b, d, f, h, j, l, n, p) after implantation. (For interpretation of the references to colour in this figure legend, the reader is referred to the Web version of this article.)

microscope of the samples. It could be seen that all samples exhibited rough surface. Fig. 2(e–l) revealed the SEM images of the samples (SPK, SNP, TAP and STP). The micropores ranging from 0.5 to 3 μm were found on the sample surface. Moreover, both Ta particles (size of ~0.1 μm) and SN particles (size of ~0.5 μm) were found to disperse onto the microporous surface.

Fig. 3 (a, b, c, d) revealed the EDS elemental spectra of the samples. The intensity of carbon (C) peak of SNP, TAP and STP spectra decreased compared with that of SPK, while the peak of Ta was found in TAP and STP, and the peaks of Si and N were found in SNP and STP. In addition, the intensity of sulfur (S) element was relatively low in all EDS spectra.

Fig. 3(e–p) revealed the EDS elemental mapping of the samples. The signal dots of the S element were relatively low on SPK, SNP, TAP and STP, confirming few sulfur elements were present on the samples. Moreover, a large number of Ta signal dots were found to disperse on TAP and STP, and a large number of Si signal dots on SNP and STP. The content of the Ta element on STP was lower than TAP, and the content of the Si element on STP was lower than SNP.

3.3. Surface roughness, hydrophilicity, surface energy and protein adsorption

Fig. 4a showed the surface roughness of samples. The average surface roughness of SPK, SNP, TAP and STP was 2.86, 3.67, 5.38 and 4.90 μm, respectively. The water contact angle (WCA) of samples was indicated in Fig. 4b. The average WCA of SPK, SNP, TAP and STP was 90.0°, 77.0°, 51.5° and 56.5°, respectively. The diiodomethane contact angle (DCA) of samples was indicated in Fig. 4c. The average DCA of SPK, SNP, TAP and STP was 66.0°, 56.0°, 25.0° and 31.0°, respectively. The surface energy of the specimens was shown in Fig. 4d. The average surface energy of SPK, SNP, TAP and STP was 32.3, 40.0, 58.2 and 53.8 mJ/m^2, respectively. Fig. 4e revealed the adsorption of protein on specimens.

The average adsorption amount of BSA on SPK, SNP, TAP and STP was 3.25, 8.34, 17.29 and 12.98 μg/cm^2, respectively. Moreover, the average adsorption amount of Fn on SPK, SNP, TAP and STP was 2.08, 3.67, 8.81 and 7.85 μg/cm^2, respectively. Fig. 4f showed the change of pH value in SBF over time. No significant change of pH value (approximately stable at pH = 7.4) was observed in the SPK and TAP, whereas the pH value gradually increased over time for SNP (approximately pH = 7.7) and STP (approximately pH = 7.6) and stabilized after 10 days.

3.4. Antibacterial activity of samples in vitro

Fig. 5a showed photographs of *S. aureus* and *E. coli* colonies on agar after 24 h culture, which were dissociated from PEKK, SPK, SNP, TAP and STP. Large amounts of *S. aureus* and *E. coli* colonies were found on PEKK, indicating no antibacterial activity. However, a few colonies were seen for SPK and TAP (significantly lower antibacterial activity), while few colonies were found for SNP and STP, indicating their effective antibacterial activity. Fig. 5b showed the percent reduction of *S. aureus* and *E. coli* for the samples. Compared with PEKK, the bacteriostatic rate of SPK against *S. aureus* was 73.12% and against *E. coli* was 62.35%. Moreover, the bacteriostatic rate of SNP against *S. aureus* was 99.51% and against *E. coli* was 99.01%; the bacteriostatic rate of STP against *S. aureus* was 97.67% and against *E. coli* was 90.13%.

3.5. Cellular response in vitro

3.5.1. Cell adhesion, morphology, proliferation and ALP activity

Fig. 6 (a, b, e, f, i, j, m, n) showed the SEM images of the cells on the samples after culture for different time. At day 1, the cells on SNP, TAP and STP exhibited some filopodia while the cells on SPK showed a spherical shape with no significant filopodia. At day 3, more cells with more filopodia and lamellipodia were seen on TAP and STP than SNP,
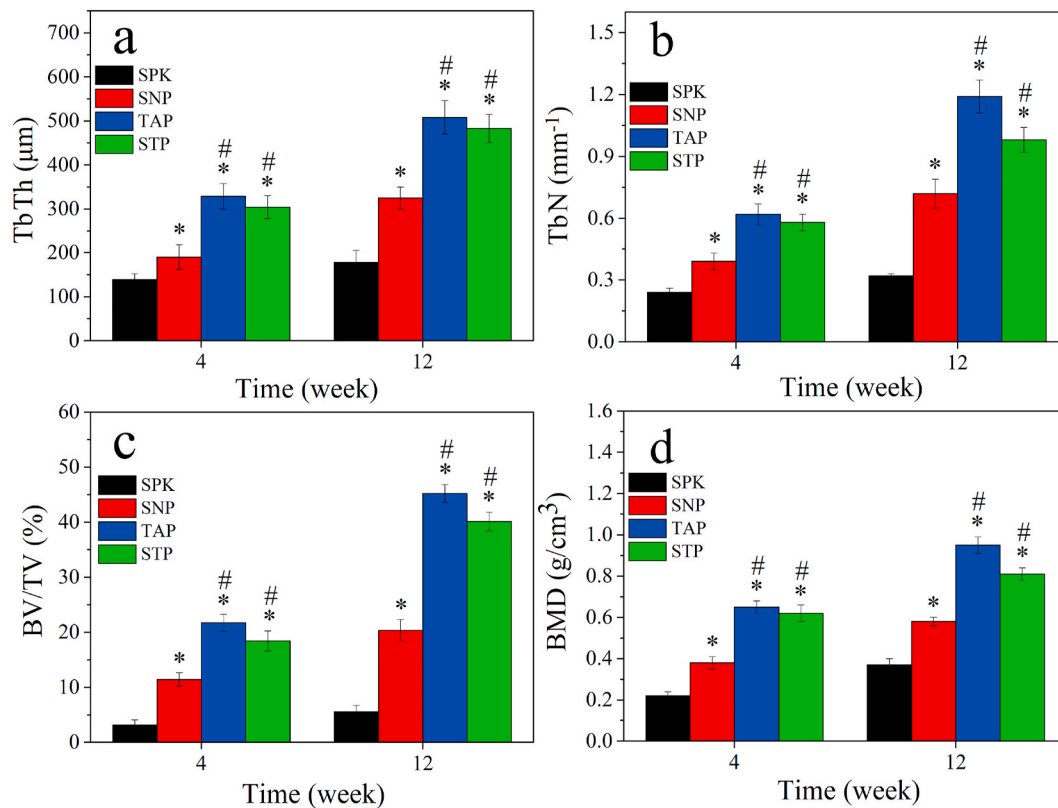
Fig. 10. Quantitative results of new bone regeneration around implants from Micro-CT at week 4 and 12 after implantation, including trabecular thickness (TbTh), trabecular number (TbN), bone volume/total volume (BV/TV) and bone mineral density (BMD) (n = 3, * was $p < 0.05$, ** was $p < 0.01$, in comparison with SPK; # was $p < 0.05$, in comparison with SNP).

and SNP than SPK. Fig. 6 (c, d, g, h, k, l, o, p) showed the cell nuclei (blue) and cytoskeleton (green) of rBMS cells on the specimens, which were stained using FITC-Phalloidin and DAPI. At day 1 after culture, the cells on SNP, TAP and STP exhibited some filopodia while the cells on SPK showed spherical shape with no significant filopodia. At day 3, more cells with filopodia and lamellipodia were found on TAP and STP than SNP, and SNP than SPK. Large amounts of cells were found on the TAP and STP surfaces while a few cells were found on SPK and SNP.

Fig. 7a showed the ALP staining images of the cells with samples at 14 days after culturing. The ALP staining for TAP and STP was stronger than SPK and SNP, indicating that the ALP activity of cells on TAP and STP was higher than SPK and SNP. Fig. 7b showed the Alizarin-Red staining images of the cells' calcium nodules with samples at 21 days after culturing. The Alizarin-Red staining of TAP and STP was stronger than SPK and SNP, indicating that the calcium nodule formation of cells on TAP and STP was higher than SPK and SNP.

Fig. 7c showed the proliferation of rBMS cells on the specimens (expressed by OD value) after culturing for different time. The cell proliferation on SNP, TAP and STP increased with time while there was no significant increase for SPK. At day 1, 3, and 7, the cell proliferation on TAP and STP was remarkably higher than that on SNP, while the cell proliferation on SNP was higher than that on SPK. Fig. 7d revealed the quantitative analysis of ALP activity of rBMS cells on the samples after culture for different time. The ALP activity of the cells on SNP, TAP, and STP increased with time, but no significant increase on SPK was observed. Moreover, at day 14, the ALP activity for TAP and STP was higher than that for SNP, while SNP exhibited higher ALP activity than SPK.

3.5.2. Osteogenic genes expressions

Fig. 7(e–h) was the osteogenic gene (ALP, OPN, OCN and Runx2) expression of cells on SPK, SNP, TAP and STP. The expression of these

genes for SNP, TAP and STP increased with time while no remarkable increase for SPK was observed. At day 3, no significant difference in ALP, OPN, OCN and Runx2 expression was found among all samples. At day 7, expression of these osteogenesis related genes for TAP and STP was higher than that for SNP and SPK, while SNP exhibited higher OPN expression than SPK. At day 14, TAP and STP showed higher expression of ALP, OCN, and Runx2 than SNP, while the expression of these genes in SNP was higher than that of SPK.

3.6. In vivo anti-infective property

3.6.1. X-ray images and anti-infective property

The X-ray images of rat femurs containing implants taken at day 14 after implantation were shown in Fig. 8a. The PEKK, SPK and TAP showed signs of osteomyelitis, presenting as obvious cortical bone destruction and periosteal reaction. The osteomyelitis and periosteal reactions were much milder for SNP and STP, suggesting good anti-infection property of SNP and STP. The implants were further harvested to evaluate their anti-infective property (Fig. 8b). Large amounts of bacteria were isolated from PEKK, SPK and TAP, whereas significantly lesser bacteria were found for both SNP and STP. Therefore, SNP and STP exhibited significantly higher anti-infective activity than SPK and TAP. Fig. 8c showed the percent reduction of *S. aureus* for the samples *in vivo*. PEKK showed no anti-infective activity while the bacteriostatic rate of SPK against *S. aureus* was 52.13%. Moreover, the bacteriostatic rate of SNP and STP against *S. aureus* was 99.23% and 90.06%, respectively.

3.7. Bone regeneration and osseointegration of implants in vivo

3.7.1. SRmCT and Micro-CT analysis

The 2D reconstructed images (SRmCT) and 3D reconstructed images (Micro-CT) of new bone (NB) tissues around the implants (SPK, SNP,
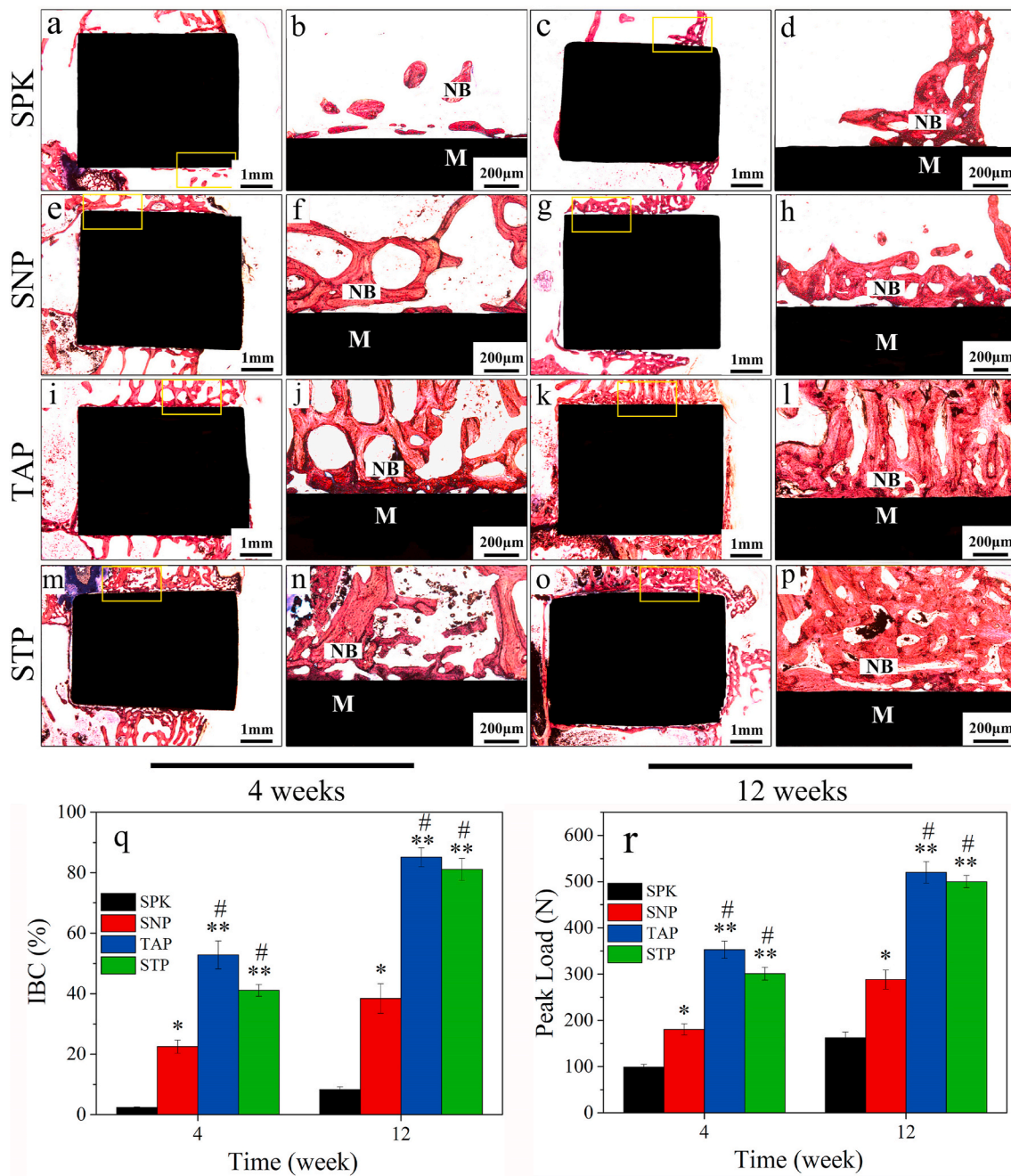
Fig. 11. Histological images (at different magnification) of SPK (a, b, c, d), SNP (e, f, g, h), TAP (i, j, k, l), and STP (m, n, o, p) at week 4 (a, b, e, f, i, j, m, n) and 12 (c, d, g, h, k, l, o, p) after implantation, and the images (b, d, f, h, j, l, n and p) are the enlarged images of small yellow frame in the images (a, c, e, g, i, k, m, o). NB represented new bone, and M represented materials. Quantitative results of implant-bone contact (q) and push-out load (r) of implants (SPK, SNP, TAP and STP) after implantation for 4 and 12 weeks (n = 3, * was $p < 0.05$, ** was $p < 0.01$, compared with SPK; # was $p < 0.05$, in comparison with SNP). (For interpretation of the references to colour in this figure legend, the reader is referred to the Web version of this article.)

TAP and STP) after implantation for different time were shown in Fig. 9. The amounts of NB around the samples increased with the implantation time. Moreover, after implantation for 4 and 12 weeks, the amounts of NB tissues around the TAP and STP implants were higher than that of SNP and SPK. Moreover, the amount of NB for TAP was the highest while that of SPK was the lowest among all groups.

The quantitative results of new bone regeneration around implants at different time after implantation, including trabecular thickness (TbTh), trabecular number (TbN), bone volume/total volume (BV/TV), and bone mineral density (BMD) were shown in Fig. 10. The new bone regeneration (TbTh, TbN, BV/TV and BMD) for SNP, TAP and STP increased with time while no significant change for SPK was found. At

week 4 and 12 after implantation, the new bone regeneration for TAP and STP was higher than that for SPK and SNP. Moreover, the new bone regeneration for TAP was the highest while SPK was the lowest among all groups.

3.7.2. Histological, implant-bone contact, and push-out load evaluation

Fig. 11(a–p) was the histological images after implantation for different time. At week 4 and 12, a more considerable amount of NB tissues was seen on the surface of both TAP and STP, while only a few NB tissues were seen for SPK. Moreover, at week 12, a clear gap at the interface between SPK and NB was seen while the NB tissues were in close contact with TAP and STP without gaps, demonstrating favorable

osseointegration.

Fig. 11q showed the quantitative analysis of implant-bone contact (IBC) after implantation for different time. The IBC for SNP, TAP and STP significantly increased from week 4–12 after implantation, while no noticeable increase for SPK was observed. At week 4 and 12, the IBC for SNP, TAP and STP was remarkably higher than that of SPK. Moreover, the IBC for TAP and STP was higher than that for SNP, while TAP was slightly higher than STP. Fig. 11r revealed the push-out load (POL) of implants after implantation for different time. The POL for SNP, TAP and STP increased from week 4–12, while there was a little increase for SPK. At week 4 and 12, the POL for SNP, TAP and STP was significantly higher than SPK. Moreover, the POL for TAP and STP was higher than that for SNP, and TAP had slightly higher POL than STP.

4. Discussion

PEKK is a promising implantable material for load-bearing bone replacement owing to its superior mechanical strength, biocompatibility and biostability. However, the bioinert nature and hydrophobicity of PEKK limit its efficiently integration with host bone tissue, which can cause the loosening and ultimate failure of implantation [9]. Both Ta and SN possess excellent outstanding osteogenic activity and can be integrated with the host bone, while SN possesses additional outstanding antibacterial activity [27,30]. To design a PEKK-based implantable material with the dual biofunctions of superior osteogenic activity for bone regeneration and antibacterial activity for preventing infection, a microporous surface containing SN/Ta microparticles was fabricated on PEKK (STP) by sulfonation in this study. Surface roughness of biomaterials is a crucial factor influencing the cell behavior, for example, microrough structure can be used as cell-anchoring sites for cell adhesion [31]. In this study, SPK exhibited a microporous surface without particles, while SNP, TAP and STP revealed microporous surfaces containing SN or/and Ta particles. Micropores ranging from 0.5 μm to 3 μm appeared on the surface of SPK, SNP, TAP and STP, and Ta particles (size of ~0.1 μm) or/and SN particles (size of ~0.5 μm) dispersed onto the microporous surface of SNP, TAP and STP. Due to the microporous surface containing SN particles, the surface roughness of SNP was higher than that of SPK. Further, in comparison with SNP, the surface roughness of STP and TAP remarkably increased because the improvement of surface roughness for Ta was higher than SN particles.

Hydrophilicity has significant effects on the biological performances of implantable materials, for example, hydrophilic surfaces can facilitate the early stages of cell adhesion and proliferation [32]. In this study, due to the microporous surface containing SN particles, the surface hydrophilicity of SNP was higher than that of SPK. In addition, in comparison with SNP, the hydrophilicity of STP and TAP increased significantly because the hydrophilicity of Ta particles was higher than that of SN. The surface energy is another surface characteristic of implantable materials known to affect the biological response, for example, a surface with high surface energy would adsorb more proteins in biological environment, which is beneficial for further attracting surrounding cells [33]. In this study, the surface energy of SNP was higher than that of SPK due to the microporous surface containing SN particles. Also, in comparison with SNP, the surface energy of STP and TAP remarkably increased because the surface energy of Ta was higher than that of SN particles.

The protein adsorption on the surface of implantable materials is beneficial to initial cell adhesion/spreading and proliferation because the adsorbed proteins function as ligands and bind to the membrane protein receptor (e.g., integrins) of cells [34,35]. In this study, because of the microporous surface containing SN particles, the protein adsorption of SNP was significantly higher than that of SPK. In addition, in comparison with SNP, STP and TAP exhibited greater protein adsorption because Ta had greater adsorption capacity than SN particles. The results of the previous discussion suggested that incorporating SN or Ta or SN/Ta particles into the microporous surface of PEKK could improve the surface properties (hydrophilicity, surface energy, roughness and protein adsorption); further, Ta was better than SN particles for improvement of surface properties.

Bacteria can easily adhere to the surface of implantable materials, and colonize to produce bacterial biofilm, which can cause inflammatory reaction, and ultimately lead to failure of implantation [15]. Biomedical materials with antibacterial activity can suppress bacterial infection, guaranteeing long-term stability of implantation [36]. In this study, PEKK showed no antibacterial activity, while after sulfonation, SPK with a few –SO_3H groups and TAP with Ta particles exhibited low antibacterial activity, because –SO_3H groups and the Ta particles possessed low antibacterial activity. However, both SNP and STP exhibited outstanding antibacterial activity against *S. aureus* and *E. coli* due to their microporous surface containing SN particles with excellent antibacterial activity. The bacteriostatic rate of STP was lower than that of SNP due to the microporous surface of STP containing fewer SN particles. Previous studies have shown that SN possessed excellent antibacterial activity because of the presence of amino (-NH_2) groups, which could form –NH_3^+ (positively charged) in a weakly acidic solution (bacterial growth micro-environment) [23,25]. The bacteria were generally negatively charged; thus, the interaction of negatively charged bacteria with positively charged –NH_3^+ groups on SN could lead to disruption and lysis of the bacterial membrane [22,23,25]. Furthermore, the dissolution of SN could cause a weak alkaline microenvironment, which inhibited bacterial growth [25,28,37]. In this study, our results also demonstrated that both SNP and STP created a weak alkaline solution after soaking in SBF.

The adhesion and proliferation of cells on implants generally depend on the surface feature (e.g., morphology, composition, hydrophilicity, roughness, surface energy and proteins adsorption) [38]. Cell adhesion and spreading on the implant surface are crucial for subsequent cell proliferation and differentiation [39]. In this study, the adhesion of rBMS cells on TAP and STP was better than that on SNP, and SNP was better than SPK. Further, the proliferation of rBMS cells on TAP and STP was higher than SNP, and SNP was higher than SPK. Clearly, the improvements of cell adhesion and proliferation on STP (in comparison with SPK) were due to the microporous surface containing both SN and Ta particles. Moreover, the cell adhesion and proliferation on TAP were higher than SNP, indicating that Ta was more favorable for cell adhesion and proliferation than SN because of its beneficial surface properties for cellular responses.

To investigate the osteogenic differentiation of rBMS cells on the samples, ALP staining and Alizarin-Red staining were evaluated, and the results revealed that the ALP and calcium nodule formation of cells on TAP and STP was higher than SNP and SPK, and SNP was higher than SPK. Moreover, ALP is the main osteogenic mark, and the improvement of ALP activity is a vital event occurring during the early period of osteogenesis [40]. Therefore, the ALP activity of the cells was determined, and the results indicated that the ALP activity of the cells on TAP and STP was higher than SNP, and SNP was higher than SPK. Furthermore, ALP, OPN, OCN and Runx2 are the essential osteogenic-related genes of osteoblasts, and improved expressions of these genes indicated osteogenic differentiation [41]. In our study, the Runx2, ALP, OPN and OCN expressions for TAP and STP were significantly higher than that of SNP, and SNP was higher than SPK. Therefore, the improvements of osteogenic differentiation of the rBMS cells on SNP were due to the microporous surface containing SN particles, while the further improvements of osteogenic differentiation for TAP and STP was attributed to the microporous surface containing Ta particles. Furthermore, osteogenic differentiation of cells cultured on TAP were higher than that on SNP, indicating that Ta could promote osteogenic differentiation better than SN due to the high surface reactivity of Ta.

The *in vivo* anti-infective property of STP was evaluated by establishing the rat femur intramedullary nail infection prevention model. The results revealed that compared with PEKK, the improvement of anti-infective property for SPK and TAP was because of the sulfonate

introduced by sulfonation. Moreover, the significant improvement of anti-infective property *in vivo* for SNP and STP was attributed to the microporous surface containing SN particles. The bacteriostatic rate of SNP was higher than STP due to the microporous surface of SNP containing more SN particles than STP. The results of the *in vitro* anti-antibacterial property were consistent with *in vivo* infective property of the samples.

The *in vivo* investigation was performed using an animal model to evaluate the influence of STP on new bone regeneration and osseointegration. From 2D and 3D reconstructed images as well as quantitative results of NB (TbTh, TbN, BV/TV and BMD) around the implants after implantation, the results revealed that NB regeneration for SNP was higher than SPK owing to the presence of SN particles, while the increases of NB regeneration for TAP and STP were because of the microporous surface containing Ta particles. The NB regeneration for TAP was higher than SNP, indicating that Ta promoted NB regeneration better than SN. Osseointegration is a chemical-biological process, in which stable anchorage of bone tissues with implants could be achieved [42]. The osseointegration of implants was examined by push-out load (POL) for different implantation time. In comparison with SPK, SNP exhibited a higher POL owing to the microporous surface containing SN particles, while the increase of POL for STP was induced by the microporous surface containing Ta particles. Furthermore, the POL for TAP was higher than that of SNP, indicating that Ta could enhance better osseointegration than SNP. For bone implants, it is pivotal to achieve a close integration with host bone tissue that guaranteed the quality of osseointegration for long-term success of implants, which could be evaluated by implant-bone contact (IBC) [43]. In the present study, the histological images showed a clear gap at the interface between SPK and bone tissue (no osseointegration). In contrast, the bone tissue was in close combination with TAP and STP without gaps at week 12, revealing favorable osseointegration. Further, the IBC for SNP was higher than SPK, and STP was higher than SNP. Moreover, the IBC for TAP was higher than SNP, indicating that Ta promoted the osseointegration better than SN.

The surface properties (e.g., morphology, composition, hydrophilicity and roughness) of implantable materials remarkably affect osteoblast response as well as bone regeneration around implants and osseointegration [44]. In our study, the presence of SN particles on SNP improved surface properties that played crucial roles in activating the response of rBMS cells *in vitro*, and thereby promoting bone regeneration and osseointegration *in vivo*. Moreover, in comparison with SNP, the presence of Ta on TAP and STP further improved surface properties, thereby further promoting the cellular response *in vitro* as well as bone regeneration and osseointegration *in vivo*. In addition, the improvements of response of rBMS cells *in vitro* and bone regeneration and osseointegration *in vivo* for TAP with Ta were greater than SNP with SN, indicating the higher osteogenic bioactivity of Ta than SN. However, SN has not only osteogenic bioactivity but also possesses antibacterial activity. As a result, incorporating of both Ta and SN particles into the microporous surface of PEKK created a new implantable material of STP with the dual biofunctions of excellent osteogenic and antibacterial activity. Therefore, STP with excellent osteogenic activity activated cellular response, and enhanced osseointegration while preventing infection, showing great potential for bone replacement.

5. Conclusions

PEKK was treated utilizing concentrated sulfuric acid suspension with both SN and Ta microparticles, and a microporous surface containing SN/Ta particles on sulfonated PEKK (STP) was fabricated. In comparison with SPK, the surface properties (hydrophilicity, roughness, surface energy and proteins adsorption) of STP significantly increased due to the presence of SN/Ta particles on the microporous surface. In addition, STP exhibited outstanding antibacterial activity, which inhibited bacterial growth *in vitro* and prevented bacterial infection *in*

vivo due to the presence of SN particles. STP also significantly activated the response (adhesion, proliferation and differentiation) of rBMS cells *in vitro*. Furthermore, STP obviously improved new bone regeneration and osseointegration *in vivo*. In conclusion, because of the incorporation of SN/Ta particles into the microporous surface, STP with optimized surface properties significantly activated cellular responses *in vitro* while promoting osseointegration and preventing infection *in vivo*. The microporous surface containing SN/Ta particles of STP exhibited excellent dual biofunction of antibacterial and osteogenic activity, which showed great potential for bone replacement.

Declaration of competing InterestCOI

The authors declare no conflict of interest.

CRediT authorship contribution statement

Xinglong Hu: Investigation, Conceptualization, Methodology, Formal analysis, Writing – original draft. **Shiqi Mei:** Visualization, Formal analysis, Data curation. **Fan Wang:** Validation, Methodology. **Songchao Tang:** Investigation, Formal analysis. **Dong Xie:** Methodology, Resources. **Chao Ding:** Investigation, Formal analysis. **Wenli Du:** Investigation, Methodology. **Jun Zhao:** Methodology, Resources, Data curation, Writing – review & editing. **Lili Yang:** Conceptualization, Methodology, Formal analysis, Visualization. **Zhaoying Wu:** Resources, Validation. **Jie Wei:** Supervision, Writing – review & editing, Project administration.

References

[1] B. Yuan, Q. Cheng, R. Zhao, X. Zhu, X. Yang, X. Yang, K. Zhang, Y. Song, X. Zhang, Comparison of osteointegration property between PEKK and PEEK: effects of surface structure and chemistry, Biomaterials 170 (2018) 116–126.

[2] X. Yang, J. Zhao, K. Wu, M. Yang, J. Wu, X. Zhang, X. Zhang, Q. Li, Making a strong adhesion between polyetherketoneketone and carbon nanotube fiber through an electro strategy, Compos. Sci. Technol. 177 (2019) 81–87.

[3] X. Feng, H. Yu, H. Liu, X. Yu, Z. Feng, S. Bai, Y. Zhao, Three-dimensionally-printed Polyether-ether-ketone implant with a cross-linked structure and acid-etched microporous surface promotes integration with soft tissue, Int. J. Mol. Sci. 20 (2019) 3811.

[4] B. Yuan, Y. Chen, H. Lin, Y. Song, X. Yang, H. Tang, E. Xie, T. Hsu, X. Yang, X. Zhu, K. Zhang, X. Zhang, Processing and properties of bioactive surface-porous PEKK, ACS Biomater. Sci. Eng. 2 (2016) 977–986.

[5] T. Choupin, B. Fayolle, G. Regnier, C. Paris, J. Cinquin, B. Brule, A more reliable DSC-based methodology to study crystallization kinetics: application to poly(ether ketone ketone) (PEKK) copolymers, Polymer 155 (2018) 109–115.

[6] Y. Damestani, D. Galan-Hoffman, D. Ortiz, P. Cabrales, G. Aguilar, Inflammatory response to implantation of transparent nanocrystalline yttria-stabilized zirconia using a dorsal window chamber model, Nanomed. Nanotechnol. Biol. Med. 12 (2016) 1757–1763.

[7] A. Gao, Q. Liao, L. Xie, G. Wang, W. Zhang, Y. Wu, P. Li, M. Guan, H. Pan, L. Tong, P. Chu, H. Wang, Tuning the surface immunomodulatory functions of polyetheretherketone for enhanced osseointegration, Biomaterials 230 (2020), 119642.

[8] R. Agarwal, C. Gonzalez-Garcia, B. Torstrick, R. Guldberg, M. Salmeron-Sanchez, A. Garcia, Simple coating with fibronectin fragment enhances stainless steel screw osseointegration in healthy and osteoporotic rats, Biomaterials 63 (2015) 137–145.

[9] W. Hong, F. Guo, J. Chen, X. Wang, X. Zhao, P. Xiao, Bioactive glass-chitosan composite coatings on PEEK: effects of surface wettability and roughness on the interfacial fracture resistance and in vitro cell response, Appl. Surf. Sci. 440 (2018) 514–523.

[10] T. Gultan, M. Yurtsever, M. Gumusderelioglu, NaOH-etched/boron-doped nanohydroxyapatite-coated PEEK implants enhance the proliferation and differentiation of osteogenic cells, Biomed. Materials 15 (2020), 035019.

[11] Y. Du, L. Zhang, X. Ye, H. Nie, Z. Hou, T. Zeng, G. Yan, P. Shang, In vitro and in vivo evaluation of bone morphogenetic protein-2 (BMP-2) immobilized collagen-coated polyetheretherketone (PEEK), Front. Mater. Sci. 9 (2015) 38–50.

[12] X. Xu, Y. Li, L. Wang, Y. Li, J. Pan, X. Fu, Z. Luo, Y. Sui, S. Zhang, L. Wang, Y. Ni, L. Zhang, S. Wei, Triple-functional polyetheretherketone surface with enhanced bacteriostasis and anti-inflammatory and osseointegrative properties for implant application, Biomaterials 212 (2019) 98–114.

[13] Z. Xue, Z. Wang, A. Sun, J. Huang, W. Wu, M. Chen, X. Hao, Z. Huang, X. Lin, S. Weng, Rapid construction of polyetheretherketone (PEEK) biological implants incorporated with brushite (CaHPO4 center dot 2H(2)O) and antibiotics for anti-infection and enhanced osseointegration, Mater. Sci. Eng. C-Mater. Biol. Appl. 111 (2020), 110782.

[14] Z. Liu, S. Ma, S. Duan, X. Deng, Y. Sun, X. Zhang, X. Xu, B. Guan, C. Wang, M. Hu, X. Qi, X. Zhang, P. Gao, Modification of titanium substrates with chimeric peptides comprising antimicrobial and titanium-binding motifs connected by linkers to inhibit biofilm formation, ACS Appl. Mater. Interfaces 8 (2016) 5124–5136.

[15] T. Koutouzis, C. Eastman, S. Chukkapalli, H. Larjava, L. Kesavalu, A novel rat model of polymicrobial peri-implantitis: a preliminary study, J. Periodontol. 88 (2017) E32–E41.

[16] X. Wei, B. Liu, G. Liu, F. Yang, F. Cao, X. Dou, W. Yu, W. Yu, B. Wang, G. Zheng, L. Cheng, Z. Ma, Y. Zhang, J. Yang, Z. Wang, J. Li, D. Cui, W. Wang, H. Xie, L. Li, F. Zhang, W. Lineaweaver, D. Zhao, Mesenchymal stem cell-loaded porous tantalum integrated with biomimetic 3D collagen-based scaffold to repair large osteochondral defects in goats, Stem Cell Res. Ther. 10 (2019) 72.

[17] E. Gee, R. Jordan, J. Hunt, A. Saithna, Current evidence and future directions for research into the use of tantalum in soft tissue re-attachment surgery, J. Mater. Chem. B 4 (2016) 1020–1034.

[18] W. Huo, L. Zhao, S. Yu, Z. Yu, P. Zhang, Y. Zhang, Significantly enhanced osteoblast response to nano-grained pure tantalum, Sci. Rep. 7 (2017) 40868.

[19] L. Wang, X. Hu, X. Ma, Z. Ma, Y. Zhang, Y. Lu, X. Li, W. Lei, Y. Feng, Promotion of osteointegration under diabetic conditions by tantalum coating-based surface modification on 3-dimensional printed porous titanium implants, Colloids Surf. B Biointerfaces 148 (2016) 440–452.

[20] H. Wang, K. Su, L. Su, P. Liang, P. Ji, C. Wang, Comparison of 3D-printed porous tantalum and titanium scaffolds on osteointegration and osteogenesis, Mater. Sci. Eng. C-Mater. Biol. Appl. 104 (2019) 109908.

[21] F. Wang, C. Li, S. Zhang, H. Liu, Tantalum coated on titanium dioxide nanotubes by plasma spraying enhances cytocompatibility for dental implants, Surf. Coating. Technol. 382 (2020), 125161.

[22] T. Webster, A. Patel, M. Rahaman, B. Bal, Anti-infective and osteointegration properties of silicon nitride, poly(ether ether ketone), and titanium implants, Acta Biomater. 8 (2012) 4447–4454.

[23] H. Wu, L. Yang, J. Qian, D. Wang, Y. Pan, X. Wang, S. Nabanita, T. Tang, J. Zhao, J. Wei, Microporous coatings of PEKK/SN composites integration with PEKK exhibiting antibacterial and osteogenic activity, and promotion of osseointegration for bone substitutes, ACS Biomater. Sci. Eng. 5 (2019) 1290–1301.

[24] R. Bock, B. McEntire, B. Bal, M. Rahaman, M. Boffelli, G. Pezzotti, Surface modulation of silicon nitride ceramics for orthopaedic applications, Acta Biomater. 26 (2015) 318–330.

[25] Z. Xu, H. Wu, F. Wang, R. Kaewmanee, Y. Pan, D. Wang, P. Qu, Z. Wang, G. Hu, J. Zhao, R. Zhao, J. Wei, A hierarchical nanostructural coating of amorphous silicon nitride on polyetheretherketone with antibacterial activity and promoting responses of rBMSCs for orthopedic applications, J. Mater. Chem. B 7 (2019) 6035–6047.

[26] G. Pezzotti, R. Bock, B. McEntire, T. Adachi, E. Marin, F. Boschetto, W. Zhu, O. Mazda, S. Bal, In vitro antibacterial activity of oxide and non-oxide bioceramics for arthroplastic devices: I. In situ time-lapse Raman spectroscopy, Analyst 143 (2018) 3708–3721.

[27] M. Ishikawa, K. Bentley, B. McEntire, B. Bal, E. Schwarz, C. Xie, Surface topography of silicon nitride affects antimicrobial and osseointegrative properties

[28] R. Bock, E. Jones, D. Ray, B. Bal, G. Pezzotti, B. McEntire, Bacteriostatic behavior of surface modulated silicon nitride in comparison to polyetheretherketone and titanium, J. Biomed. Mater. Res. 105 (2017) 1521–1534.

[29] Z. Tan, J. Sun, C. Wu, J. Qiu, C. Liu, Phosphorus-containing polymers from THPS. IV: Synthesis and properties of phosphorus-containing polybenzoxazines as a green route for recycling toxic phosphine (PH3) tail gas, J. Hazard Mater. 322 (2017) 540–550.

[30] X. Hu, S. Mei, F. Wang, J. Qian, D. Xie, J. Zhao, L. Yang, Z. Wu, J. Wei, Implantable PEKK/tantalum microparticles composite with improved surface performances for regulating cell behaviors, promoting bone formation and osseointegration, Bioact. Mater. 6 (2021) 928–940.

[31] Y. Jo, B. Choi, C. Kim, H. Cha, Diatom-inspired silica nanostructure coatings with controllable microroughness using an engineered mussel protein glue to accelerate bone growth on titanium-based implants, Adv. Mater. 29 (2017), 1704906.

[32] K. Cheon, C. Park, M. Kang, I. Kang, M. Lee, H. Lee, H. Kim, H. Jung, T. Jang, Construction of tantalum/poly(ether imide) coatings on magnesium implants with both corrosion protection and osseointegration properties, Bioact. Mater. 6 (2021) 1189–1200.

[33] A. Raines, M. Berger, Z. Schwartz, B. Boyan, Osteoblasts grown on microroughened titanium surfaces regulate angiogenic growth factor production through specific integrin receptors, Acta Biomater. 97 (2019) 578–586.

[34] J. Sefkow-Werner, P. Machillot, A. Sales, E. Castro-Ramirez, M. Degardin, D. Boturyn, E.A. Cavalcanti-Adam, C. Albiges-Rizo, C. Picart, E. Migliorini, Heparan sulfate co-immobilized with cRGD ligands and BMP2 on biomimetic platforms promotes BMP2-mediated osteogenic differentiation, Acta Biomater. 114 (2020) 90–103.

[35] S. Wu, X. Liu, C. Gao, Role of adsorbed proteins on hydroxyapatite-coated titanium in osteoblast adhesion and osteogenic differentiation, Sci. Bull. 60 (2015) 691–700.

[36] F. Liu, X. Wang, T. Chen, N. Zhang, Q. Wei, J. Tian, Y. Wang, C. Ma, Y. Lu, Hydroxyapatite/silver electrospun fibers for anti-infection and osteoinduction, J. Adv. Res. 21 (2020) 91–102.

[37] Y. Dai, H. Guo, L. Chu, Z. He, M. Wang, S. Zhang, X. Shang, Promoting osteoblasts responses in vitro and improving osteointegration in vivo through bioactive coating of nanosilicon nitride on polyetheretherketone, J. Orthop. Transl. 24 (2020) 198–208.

[38] R. Muzzarelli, M. El Mehtedi, C. Bottegoni, A. Gigante, Physical properties imparted by genipin to chitosan for tissue regeneration with human stem cells: a review, Int. J. Biol. Macromol. 93 (2016) 1366–1381.

[39] I. Lauria, T. Kutz, F. Boeke, S. Rutten, D. Zander, H. Fischer, Influence of nanoporous titanium niobium alloy surfaces produced via hydrogen peroxide oxidative etching on the osteogenic differentiation of human mesenchymal stromal cells, Mater. Sci. Eng. C-Mater. Biol. Appl. 98 (2019) 635–648.

[40] C. Wiraja, D. Yeo, M. Chong, C. Xu, Nanosensors for continuous and noninvasive monitoring of mesenchymal stem cell osteogenic differentiation, Small 12 (2016) 1342–1350.

[41] Z. Tang, T. Xu, Y. Li, W. Fei, G. Yang, Y. Hong, Inhibition of CRY2 by STAT3/miRNA-7-5p promotes osteoblast differentiation through upregulation of CLOCK/BMAL1/P300 expression, Mol. Ther. Nucleic Acids 19 (2020) 865–876.

[42] S. Goodman, Z. Yao, M. Keeney, F. Yang, The future of biologic coatings for orthopaedic implants, Biomaterials 34 (2013) 3174–3183.

[43] B. Li, P. Gao, H. Zhang, Z. Guo, Y. Zheng, Y. Han, Osteoimmunomodulation, osseointegration, and in vivo mechanical integrity of pure Mg coated with HA nanorod/pore-sealed MgO bilayer, Biomater. Sci. 6 (2018) 3202–3218.

[44] W. Chrzanowski, J. Lee, A. Kondyurin, M. Lord, J. Jang, H. Kim, M. Bilek, Nano-bio-chemical braille for cells: the regulation of stem cell responses using Bi-functional surfaces, Adv. Funct. Mater. 25 (2015) 193–205.

of tibial implants in a murine model, J. Biomed. Mater. Res. 105 (2017) 3413–3421.